Fast computation of time-domain scattering by an inhomogeneous stratified seafloor

Derek R. Olson, and Charles W. Holland

Citation: The Journal of the Acoustical Society of America **147**, 191 (2020); doi: 10.1121/10.0000570
View online: https://doi.org/10.1121/10.0000570
View Table of Contents: https://asa.scitation.org/toc/jas/147/1
Published by the Acoustical Society of America

JASA ARTICLE

Fast computation of time-domain scattering by an inhomogeneous stratified seafloor

Derek R. Olson[1,a)] and Charles W. Holland[2]
[1]Oceanography Department, Naval Postgraduate School, Monterey, California 93943, USA
[2]Applied Research Laboratory, The Pennsylvania State University, State College, Pennsylvania 16804, USA

ABSTRACT:
Marine sediment properties exhibit fluctuations on a very wide range of scales in all three spatial dimensions. These fluctuations lead to scattering of acoustic waves. Seabed scattering models that treat such fluctuations are reasonably well developed under the plane-wave assumption. A recent model, called TDSS (time domain model for seafloor scattering), accurately treats the important point-source-point-receiver geometry for generally stratified fluid sediments—important because this is the geometry employed in many seabed scattering measurements. The computational cost associated with this model is very high and scales roughly with the product of mean source-receiver height above the basement to the fifth power and both bandwidth and wavenumber to the second power. Thus, modeling deep ocean scattering from a near sea surface source and receiver is prohibitive at frequencies above a few tens of hertz. A computational approach was developed based on Levin's method of oscillatory integration, which is orders of magnitude faster than standard numerical integration techniques and makes deep ocean seabed scattering computations practical up to many kilohertz. This approach was demonstrated to agree with the narrowband sonar equation in several simple environments in the limit of small bandwidths, but the TDSS model is expected to be valid for a much wider range of environments.
https://doi.org/10.1121/10.0000570
(Received 3 July 2019; revised 28 November 2019; accepted 16 December 2019; published online 22 January 2020)
[Editor: Ying-Tsong Lin] Pages: 191–204

I. INTRODUCTION

Inhomogeneities in the seafloor, including sediment layering and fluctuations, cause the scattering of sound. Scattering can be due to either the water–sediment rough interface, or from fluctuations in seafloor properties and buried sediment layers. Scattering from the latter category of inhomogeneities is known as sub-bottom scattering. In remote sensing applications, the goal is to infer the structure of the sediment from the received signal scattered or reflected by the ocean environment. This type of inference requires an accurate model for the interaction of acoustic waves with inhomogeneous sediments.

For stratified sediments, a simple, analytically tractable solution for the scattering cross section can be found if an incident plane wave is assumed (e.g., see Jackson and Richardson, 2007; Morse and Ingard, 1968; Ogilvy, 1991; Tatarski, 1961, and numerous references therein). The plane-wave incident field assumption is adequate in some experimental setups, e.g., where the incident grazing angle does not vary appreciably within the ensonified area. In many scenarios with a compact source, the plane-wave assumption is inaccurate, even when the far-field criterion for the source is met, e.g., near vertical incidence for interface scattering (Hellequin *et al.*, 2003; Jackson and Richardson, 2007, p. 502), and for cases where in the incident field the sub-bottom region contains significant curvature (Holland and Neumann, 1998). In these cases, returns from the interface, volume, and sub-bottom interfaces may not be separated in time, and each has its own intensity time-dependence. If a model is used with a plane-wave incident field it may not accurately capture the time-dependence of the received field. Thus, plane-wave quantities, such as the scattering cross section, sometimes cannot be directly estimated from short-range reverberation measurements with a point source (Tang and Frisk, 1992). More involved modeling of the experimental geometry must be performed since the geometry-dependent components in the sonar equation cannot be simply inverted for scattering strength.

One of the early full-wave models for sub-bottom scattering from a broadband point source was Tang and Frisk (1992), using a wavenumber integration approach to calculate the scattered field from individual realizations of sound speed fluctuations. Related work includes LePage and Schmidt (2000, 2003) and Schmidt and Kuperman (1995), who also used a wavenumber integral approach. Recently, Tang and Jackson (2017) derived a full-wave sub-bottom scattering model, called TDSS (time-domain model for seafloor scattering), that produces the formally averaged time-dependent mean square acoustic pressure from arbitrary roughness or volume heterogeneity spectra from a broadband point source. Apart from the perturbation assumption for scattering, Tang and Jackson's model contains no other approximations and shows modest agreement with the narrowband sonar equation for simple seafloors.

a)Electronic mail: dolson@nps.edu, ORCID: 0000-0002-7928-0468.

In this work, we show that the discrepancies between the TDSS model and the sonar equation in Tang and Jackson (2017) are due to their choice of geometry and signal parameters. Once the water depth becomes large compared to the spatial extent of the transmitted pulse, the two models show much better agreement. However, deep water environments present a computational challenge.

The TDSS model requires the evaluation of multiple nested highly oscillatory integrals. At low frequencies and for sources close to the seafloor, calculation of these integrals can be performed in a reasonable amount of time using direct numerical quadrature, or in the case of LePage and Schmidt (2003), using a fast Hankel transform. For high frequencies, and deep water scenarios in which the source and receiver altitudes are large compared to the acoustic wavelength, the computational cost in both central processing unit (CPU) time and memory becomes prohibitive.

In this work, we detail an efficient method to calculate the two-dimensional (2D) oscillatory integrals in the TDSS model using a technique from Levin (1982) and Olver (2006). We call our implementation TDSS-L. This type of numerical integration has been previously used in geoacoustic inversion of the spherical wave reflection coefficient (Quijano *et al.*, 2015), which involves a single highly oscillatory integral. The number of oscillations in the integrands depends heavily on source/receiver height above the seabed and frequency. Therefore, the computational cost of using standard numerical techniques becomes enormous for source/receiver depths near the sea surface in deep ocean environments at frequencies of hundreds or thousands of hertz. The fast integration technique described in this paper opens the door to computing the received intensity in this environment.

Several properties of the oscillatory integrals in the TDSS model prevent straightforward application of the Levin technique. The first is that the TDSS model contains weakly singular integrals, which cannot be directly used in the Levin method. We detail a method to overcome this impediment using variable transformations. The second is that the oscillatory part of the integrands in the TDSS model contains terms with variable instantaneous frequency (i.e., nonlinear phase) of the form $\exp\left[iq\sqrt{1-(K_1/k_w)^2}\right]$, where k_w is the wavenumber in water, q determines the number of oscillations, and K_1 is a variable of integration. The Levin technique has an error independent of q, but an error that increases as K_1 approaches k_w. Straightforward application of the Levin technique to this integrand can lead to large errors, and suboptimal efficiency. To mitigate this drawback, we develop a nonuniform sampling technique for the oscillatory integrals.

Large source receiver altitudes provide a strenuous test of the TDSS model and also a suitable test against the narrowband sonar equation. In Tang and Jackson (2017), modest agreement between the TDSS model and narrowband sonar equation for halfspace environments is observed. The model mismatch was larger than one would expect given the simplicity of the environment. In the present work, we present comparisons between the TDSS model and narrowband sonar equation for large source and receiver altitudes and find much better agreement. Based on results in the present work, the previous discrepancies resulted from the inadequacy of the narrowband sonar equation for small source/receiver height and wider bandwidth, since TDSS models the point source geometry and broadband scattering exactly. We also compare the TDSS model with the sonar equation for a single refracting layer, which is an important test of the physics in the TDSS model given that sediment sound speed generally increases with depth in marine sediments. These model-model comparisons are more successful than presented in Tang and Jackson (2017), and provide more evidence that TDSS is a physical sound model. Results are also given from a deep water complex turbidite environment, which contains strong stratification and cannot be accurately modeled using the sonar equation approach.

In Sec. II, the basic geometry, environmental properties, and source characteristics are given. We give an overview of the TDSS model of Tang and Jackson (2017) in Sec. III, as well as a discussion of its computational cost in terms of environmental and geometrical parameters. Numerical integration techniques are described in Sec. IV, beginning with a generic method for performing 2D integration over the domain required by the model. Then in Sec. V, fast methods for computing highly oscillatory integrals are reviewed and applied to the weakly singular integrands for the TDSS model. Results for several simple scenarios and a complex environment are given in Sec. VI with conclusions given in Sec. VII.

II. ENVIRONMENT, GEOMETRY, AND SOURCE CHARACTERISTICS

Although the TDSS model can treat scattering due to both rough interfaces and heterogeneous volumes, only interface scattering is treated here. The fast integration method presented in this work is applicable to both of these formulations since both of them employ 2D oscillatory integrals of very similar forms.

The geometry is shown in Fig. 1. The source and receiver altitudes above the water–sediment interface are specified by z_S and z_R, respectively. The seafloor consists of N fluid layers with the layer number denoted by n. The water column is taken to be $n=0$ and is a semi-infinite halfspace. Layer N is also a semi-infinite halfspace bounding the stack of layers from below, and is referred to as the "basement." The total sediment thickness above the basement is z_D. Each fluid layer, as well as the basement, is specified by its compressional phase speed $\tilde{c}_{pn}$ in m/s, density ρ_n in kg/m^3, and attenuation α_{pn} in dB/m/kHz. The acoustic angular frequency is ω, and the wavenumber in water is $k_w = \omega/c_w$, where c_w is the speed of sound in water. The wavenumber in each sediment layer is $k_n = k_w a_{pn}^{-1}$, where a_{pn} is the ratio between the complex sound speed in layer n and the sound speed in water. Complex sound speed

https://doi.org/10.1121/10.0000570

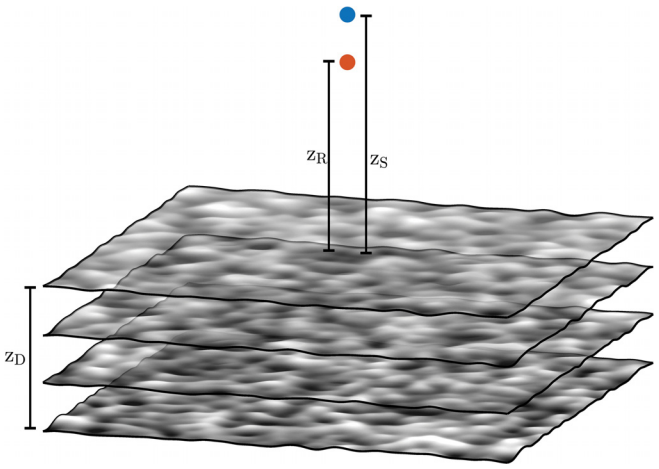

FIG. 1. (Color online) An example of the TDSS model environment with a three-layer sediment, a basement halfspace, and overlying water column. The source and receiver heights are shown as well as the total sediment thickness above the basement.

is computed using $c_{pn} = \tilde{c}_{pn}/(1 + i\delta_{pn})$, where $\delta_{pn} = \alpha_{pn}\tilde{c}_{pn}\log(10)/(4 \times 10^4\pi)$ is a dimensionless loss parameter. The density ratio, $a_{\rho n}$, is the density of each layer divided by the density of water.

Each interface between fluid layers can have an arbitrary roughness spectrum. For simplicity, here, we assume an isotropic roughness power spectrum of the von Kármán type given by

$$W_n(K) = \frac{w_2}{(L^{-2} + K^2)^{\gamma_2/2}}, \tag{1}$$

where W_n is the roughness power spectrum of interface n, K is the magnitude of the transverse wave vector, w_2 is the spectral strength with units of $\mathrm{m}^{4-\gamma_2}$, γ_2 is the spectral exponent, and L is the outer scale with units of m. Note that K is used for the spatial wavenumber of the roughness and not the acoustic wavenumber.

The pulse transmitted by the source is assumed to be a complex analytic signal, $s(t)$, with a complex amplitude spectrum, $S(\omega)$, given by

$$S(\omega) = \int \mathrm{d}t\, s(t) e^{i\omega t}. \tag{2}$$

In the numerical examples given in Sec. VI, a Gaussian pulse is used with the amplitude spectrum given by

$$S(\omega) = \frac{\sqrt{2\pi}}{2\Delta\omega} e^{-(\omega-\omega_0)^2/2(\Delta\omega)^2}, \tag{3}$$

where

$$\Delta\omega = \frac{\pi W_{3\mathrm{dB}}}{\sqrt{\log 2}} \tag{4}$$

has units of rad/s and is proportional to the half power full bandwidth, $W_{3\mathrm{dB}}$, with units of Hz. To compare to the narrowband sonar equation, the integrated pressure squared, E, of this pulse is required. We define $s(t)$ to be dimensionless and let the transmitted pulse 1 m from the source be $p(t) = p_0 s(t)$, where p_0 has units of pascals and is related to the source level. Using Parseval's theorem (Oppenheim *et al.*, 1999), we obtain

$$E = \int \mathrm{d}f\, p_0^2 |S(\omega/(2\pi))|^2 = \frac{\sqrt{\pi} p_0^2}{4W_{3\mathrm{dB}}}. \tag{5}$$

For all results presented below, a 0 dB re Pa source level is used with $W_{3\mathrm{dB}} = 2.35$ Hz. This small bandwidth is employed so that we may compare the output of the TDSS models with the narrowband sonar equation.

III. SCATTERING MODEL

A. Model description

The TDSS model (Tang and Jackson, 2017) predicts the time-dependence of the mean squared pressure $\langle |p(t)|^2 \rangle$, scattered by a stratified, rough, and heterogeneous seafloor due to the incident field produced by a broadband pulse from a point source. The model employs perturbation theory for rough fluid–fluid interfaces (Kuo, 1964) and volume heterogeneities (Ivakin, 1998). Their model extends the work by Schmidt and Kuperman (1995) for rough surface reverberation and LePage and Schmidt (2003) for volume reverberation by estimating the formally averaged second moment of the acoustic field, $\langle |p(t)|^2 \rangle$, as opposed to realizations of the scattered pressure. We also note that, in general, the TDSS model can handle general bistatic geometry, but considerable simplifications can be made if the geometry is restricted to only vertically bistatic cases. In this work, we make this restriction to the latter case. Study of the general bistatic case, as well as efficient computational algorithms appropriate to that geometry are fruitful areas for future work. The TDSS model is, at present, restricted to fluid sediment layers, but could be applied to elastic or poroelastic seafloor by using the Green's functions and their gradients for those types of environments and starting with a version of Eq. (13) in Tang and Jackson (2017) appropriate for elastic or poroelastic boundary conditions.

The use of first-order perturbation theory limits the validity of this formulation as it neglects multiple scattering between different rough interfaces, higher-order scattering from individual interfaces, assumes that the layer thickness is large compared to the mean square roughness, and neglects the effect of the roughness on the coherent background field. Multiple scattering is defined as scattering (from a rough interface) of the scattered field from another rough interface. It is important to differentiate this from multiple reflections, which is treating all orders of reflection present in the up- and down-going plane waves within a layer. We note that multiple reflections are treated exactly in this work (assuming the roughness does not affect the coherent field), but multiple scattering is ignored—a possible significant limitation of this model.

The formulas required to compute the mean square scattered pressure are reproduced here for completeness and to facilitate discussion of the computational cost dependence on the environment, geometry, and source pulse. A complete derivation of this model can be found in Tang and Jackson (2017), along with a thorough discussion of the physical interpretation of each of its components.

In the TDSS model, the mean square pressure is computed as

$$\langle |p(t)|^2 \rangle = \sum_{n=1}^{N} \langle |p_n(t)|^2 \rangle, \tag{6}$$

$$\langle |p_n(t)|^2 \rangle = 2\pi \int_0^\infty \mathrm{d}K\, W_n(K) K |h_n(K,t)|^2, \tag{7}$$

$$h_n(K,t) = \pi \int_0^\infty \mathrm{d}\omega\, S(\omega) U_n(K,\omega) e^{-i\omega t}, \tag{8}$$

$$U_n(K,\omega) = \left(\frac{k_n^2}{a_{\rho n}} - \frac{k_{n-1}^2}{a_{\rho(n-1)}} \right) g_{\kappa n}(K) - \left(\frac{1}{a_{\rho n}} - \frac{1}{a_{\rho(n-1)}} \right) \times \left[g_{\perp n}(K) + \frac{a_{\rho(n-1)}}{a_{\rho n}} g_{zn}(K) \right], \tag{9}$$

where k_n is the complex wavenumber in layer n. Note that the expression for $U_n(K,\omega)$ in Tang and Jackson (2017) [their Eq. (18)] contains a sign error that has been corrected here.

The functions $\langle |p_n(t)|^2 \rangle$ represent the scattered mean square pressure from each interface n while other layers are flat, and are summed to obtain the total mean square pressure, $\langle |p(t)|^2 \rangle$. The isotropic roughness spectra used here for each layer are given in Eq. (1). The function $h_n(K,t)$ is a transfer function that gives the complex amplitude response in the time domain for each horizontal Bragg wavenumber.

The quantities $U_n(K,\omega)$ are the frequency domain versions of $h_n(K,t)$ and do not depend on the transmitted signal. The lower case g functions represent the 2D Fourier transform of the two-way Green's function. Their general form is given by Eq. (14) in Tang and Jackson (2017). A vertically bistatic geometry with isotropic roughness results in considerable simplification. With these assumptions, the two-way Green functions can be expressed in terms of a double integral over wavenumber, which is used exclusively in this work

$$g_{\kappa n}(K,f) = -\frac{1}{2\pi} \int_0^\infty \int_0^\infty \frac{K_1\, \mathrm{d}K_1}{k_{zw}(K_1)} \frac{K_2\, \mathrm{d}K_2}{k_{zw}(K_2)} H_1(K,K_1,K_2) \times e^{ik_{zw}(K_1)z_S + ik_{zw}(K_2)z_R} D_1(K_1,z_n) D_1(K_2,z_n), \tag{10}$$

$$g_{\perp n}(K,f) = -\frac{1}{2\pi} \int_0^\infty \int_0^\infty \frac{K_1^2\, \mathrm{d}K_1}{k_{zw}(K_1)} \frac{K_2^2\, \mathrm{d}K_2}{k_{zw}(K_2)} H_2(K,K_1,K_2) \times e^{ik_{zw}(K_1)z_S + ik_{zw}(K_2)z_R} D_1(K_1,z_n) D_1(K_2,z_n), \tag{11}$$

$$g_{zn}(K,f) = \frac{a_{pn}^2}{a_{p(n-1)}^2 2\pi} \int_0^\infty \int_0^\infty \frac{K_1\, \mathrm{d}K_1}{k_{zw}(K_1)} \frac{K_2\, \mathrm{d}K_2}{k_{zw}(K_2)} \times e^{ik_{zw}(K_1)z_S + ik_{zw}(K_2)z_R} D_2(K_1,z_n) D_2(K_2,z_n) \times k_{zpn}(K_1) k_{zpn}(K_2) H_1(K,K_1,K_2), \tag{12}$$

$$D_1(K,z_n) = A_n(K) + B_n(K), \tag{13}$$

$$D_2(K,z_n) = -A_n(K) + B_n(K). \tag{14}$$

Here, $i = \sqrt{-1}$, and $k_{zw}(K) = \sqrt{k_w^2 - K^2}$ is the vertical component of the wave vector in water corresponding to the horizontal component K. The vertical component of the wavenumber in layer n is denoted $k_{zpn} = \sqrt{k_{pn}^2 - K^2}$, and in water is k_{zw}. Our Eq. (12) differs from Eq. (31) of Tang and Jackson (2017) because we used the vertical component of the wavenumber in each layer k_{zpn} instead of the sine of the grazing angle β_n. Conversion of $k_{p(n-1)}$ to k_{pn} requires the factor $a_{pn}/a_{p(n-1)}$. In these formulas, all wavenumbers (except for K) may be complex due to attenuation or an artificially introduced imaginary component of frequency. In many experimental geometries, z_R will be very close to z_S relative to the water depth, and it is useful to use the mean altitude, $z_m = (z_S + z_R)/2$.

The functions H_1 and H_2 are defined by Watson (1944, p. 411).

$$H_1 = 1/(2\pi\Delta), \tag{15}$$

$$\Delta = \frac{1}{4} \sqrt{2K^2K_1^2 + 2K^2K_2^2 + 2K_1^2K_2^2 - K^4 - K_1^4 - K_2^4}, \tag{16}$$

$$H_2 = H_1 \frac{K_1^2 + K_2^2 - K^2}{2K_1K_2} \tag{17}$$

if the scalars K, K_1, and K_2 can form the sides of a triangle, and are equal to zero if they cannot. This enforces the Bragg condition, in which each horizontal Bragg wavenumber K is matched to all possible combinations of incident and scattered horizontal acoustic wavenumbers. The function H_1 enforces the Bragg condition and is plotted for $K = 0.4$ in Fig. 2. The parameters $D_1(K,z_n)$ and $D_2(K,z_n)$ are defined in terms of the up- and down-going plane-wave amplitudes [$A_n(K)$ and $B_n(K)$, respectively] in layer n. These coefficients are defined for a unit amplitude plane-wave incident at the water–sediment interface.

The Fourier integral used in Eq. (8) is computed here using complex contour integration, in which a small positive imaginary component to ω is introduced, $\tilde{\omega} = \omega + i\delta_\omega$. The imaginary frequency is compensated by multiplying $h_n(K,t)$ by $\exp(\delta_\omega t)$ after the frequency integration is performed. As recommended by Jensen *et al.* (2011, pp. 616–617), a value of $\delta_\omega = \log(50)/T$ was used, where T is the maximum time desired. Both $U(K,\omega)$ and $S(\omega)$ are evaluated at complex frequencies, which can be performed using analytic continuation. The complex contour serves the dual purpose of attenuating aliased signals in the time

https://doi.org/10.1121/10.0000570

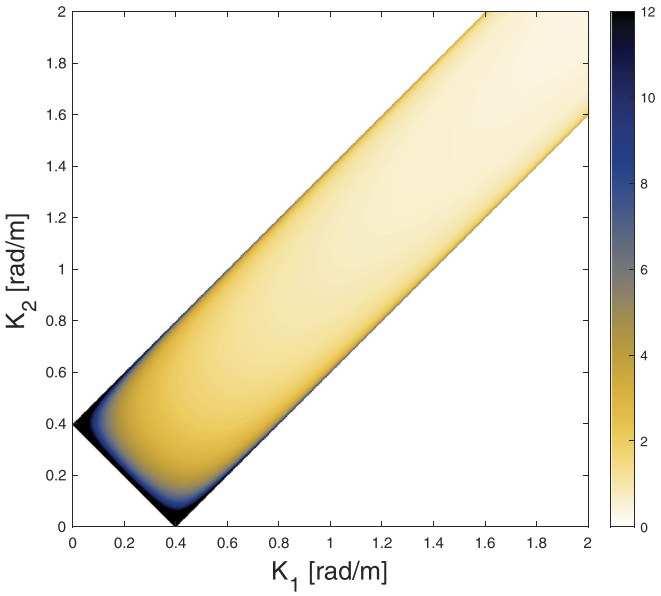

FIG. 2. (Color online) Plot of H_1, defined in Eq. (15) for $K = 0.4$ rad/m. The tilted rectangle in the middle is the domain of support for H_1 (i.e., Bragg scattering) and continues to the upper right.

domain, as well as mitigating the weak singularities due to the factors of k_{zw}^{-1} in the integrals for the g functions.

B. Computational issues

The computational cost for this model can be assessed by examining each sum or integral. The sum over layers, integral over frequency, and integral over the Bragg wavenumber are all simple to compute compared to the frequency-domain two-way Green's functions, $g_{\kappa n}$, $g_{\perp n}$, and g_{zn}. These latter functions require computation of highly oscillatory 2D integrals. Therefore, the computational burden depends on the time required to compute the g functions for a single value of n, f, and K, and the number of points at which these functions are required, which is N; N_f, the number of frequencies; and N_K, the number of wavenumbers, respectively. N is the number of sediment layers and is set by the environment. The number of frequencies is set by the bandwidth, $W_{3\text{dB}}$, and maximum time required in the simulation, T, through $N_f = W_{3\text{dB}}T$. For modeling direct-path measurements of bottom scattering down to a minimum grazing angle, $\theta_{\min}$, then $T \propto z_m$. The number of frequencies is then proportional to $W_{3\text{dB}}z_m$.

The number of Bragg wavenumbers, N_K, is set by the dependence of $h_n(K,t)$, the time-domain transfer function. If we consider a simple halfspace, then $h_n(K,t)$ will have a peak at the two-way travel time for each Bragg wavenumber, which can be related to the grazing angle, θ through $K = 2k_w \cos\theta$. Therefore, the sampling of the K axis should be fine enough such that the difference in the two-way travel time between adjacent wavenumber samples is less than the temporal width of h_n. As z_m increases, the two-way travel time between samples will increase linearly. Thus, N_K is directly proportional to z_m. Two cases of $h_n(K,t)$ for a sand halfspace example are shown in Fig. 3, one with an undersampled K axis, and one with a properly sampled one.

A longer transmitted pulse will cause the temporal width of $h_n(K,t)$ with fixed K to be increased (an example is shown in Fig. 3), allowing for coarser sampling of the wavenumber domain. Thus, N_k is directly proportional to $W_{3\text{dB}}$ so long as a zero- or linear-phase pulse is employed. N_k is proportional to T as well since for a given wavenumber spacing, longer times require that smaller grazing angles be included, up to a limit of 0°, corresponding to a Bragg wavenumber $K = 2k_w$. For finite values of T, grazing angles smaller than $\theta_{\min} = \sin^{-1}(2z_m/(cT))$ will not affect the result, and the upper limit of K can be set based on this angle. Again, since T is proportional to z_m (for direct path bottom scattering), N_k is proportional to another factor of z_m. To summarize, N_f is proportional to $W_{3\text{dB}}z_m$, and N_k is proportional to $W_{3\text{dB}}z_m^2$. Thus, the number of points at which the Green's functions must be calculated is proportional to $NW_{3\text{dB}}^2 z_m^3$.

Next, we estimate the cost of calculating a single value of the two-way Green's functions, which are 2D oscillatory integrals over an infinite domain. The support of the integrals is restricted to the support of the H_1 and H_2 functions, one of which is shown in Fig. 2. Given that the vertical wavenumbers will be evanescent when K_1 or K_2 is greater than k_w, the upper limit of the integrals can be truncated such that the exponentials decay to a sufficiently small value compared to unity.

The main difficulty in numerically evaluating these integrals is capturing the oscillations. The oscillations result from the exponential functions, as well as the D_1 and D_2 functions that are related to the plane-wave coefficients in each layer. The H_1 and H_2 functions have weak singularities at their boundaries, which also causes difficulties with numerical integration. For the complex exponential

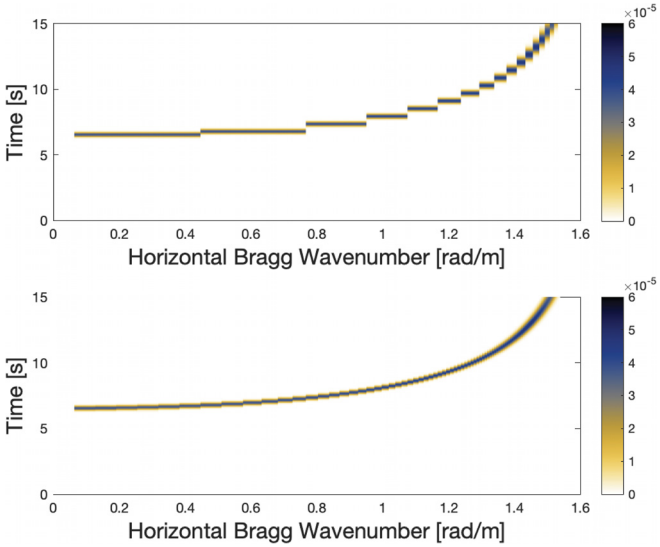

FIG. 3. (Color online) $|h_n(K,t)|$ for a sand halfspace computed with undersampled (top) and properly sampled (bottom) wavenumber axes for a Gaussian source spectrum with a 3 dB bandwidth of 2.35 Hz.

functions, the total phase change of each exponential between 0 and k_w is $k_w z_m$. Therefore, an approximate scaling of the number of quadrature points to resolve the oscillations in the product of the two exponential functions in the 2D integral is $O(k_w^2 z_m^2)$. The thicker the sediment stack compared to the average wavelength, the more peaks in A_n and B_n there will be due to modes within the sediment (Jensen *et al.*, 2011, Chap. 5). An approximate scaling for the number of oscillations in D_1 and D_2 is $O(\bar{k}_p z_D)$ for each integral, where z_D is the total sediment thickness, and $\bar{k}_p$ is the average wavenumber over all sediment layers. Typically, $\bar{k}_p$ is the same order of magnitude as k_w, so we will use $O(k_w z_D)$ instead.

Combining the results of the previous five paragraphs, the computational cost scales as $O(NW_{3\mathrm{dB}}^2 z_m^3 k_w^2 (z_m^2 + z_D^2))$. Here, we assume that k_w represents the order of magnitude of all wavenumbers. If extremely broadband simulations are required, then the analysis will be slightly different. If the average source/receiver altitude, z_m, is large compared to λ and z_D, then the computational cost will scale as $O(z_m^5)$. For deep water scenarios, z_m is $O(10^3)$, and the computational cost becomes impractical if direct numerical quadrature is employed. For such scenarios, either more computing resources could be used, or a more efficient numerical integration strategy could be employed. This work develops the latter.

The computational method developed below addresses the factors of $(k_w z_m)^2$ in the order of magnitude estimate. The number of points required for standard quadrature is approximately $N_q = (10 k_w z_m/(2\pi))^2$, if ten points per oscillation are used. For a frequency of 4000 Hz and z_m of 4900 m (parameters used in the example below), then $N_q \approx 10^{10}$. The Levin method below uses a constant number of function evaluations as a function of z_m for the 2D oscillatory integrals. In the examples presented below, this number is approximately 10^5. Thus, the Levin method provides a speedup factor of 10^5 at 4900 Hz and 10^2 at 200 Hz.

IV. NUMERICAL IMPLEMENTATION OF OSCILLATORY INTEGRALS

In this section, methods are presented to evaluate the oscillatory singular integrals over K_1 and K_2 in Eqs. (10)–(12). We first introduce a generic form for the integration kernels,

$$Q = \int\int \mathrm{d}K_1 \mathrm{d}K_2 \, \phi(K_1, K_2) e^{iq\eta(K_1,K_2)}, \tag{18}$$

where $\phi(K_1, K_2)$ is the slowly varying portion of the integration kernel, and $\eta(K_1, K_2)$ is the phase function, defined below. The dimensionless parameter $q = k_w z_m$ approximately specifies the number of oscillations in K_1 and K_2 when divided by 2π. The functions ϕ and η are different for each of g_κ, $g_\perp$, and g_z. For the case of g_κ in Eq. (10), they are

$$\phi(K_1, K2) = \frac{K_1}{k_{zw}(K_1)} \frac{K_2}{k_{zw}(K_2)} H_1(K, K_1, K_2) \times D_1(K_1, z_n) D_1(K_2, z_n), \tag{19}$$

$$\eta(K_1, K_2) = \frac{z_S}{z_m} \sqrt{1 - \frac{K_1^2}{k_w^2}} + \frac{z_R}{z_m} \sqrt{1 - \frac{K_2^2}{k_w^2}}. \tag{20}$$

Although the D_1 and D_2 functions are technically oscillatory, the Levin integration technique requires that the oscillatory terms be given explicitly (e.g., complex exponentials or Bessel functions; Levin, 1996; Quijano *et al.*, 2015).

To compute the integral, the domain is truncated such that the truncation location does not appreciably affect the result. For $K_1, K_2 \geq k_w$, the exponential term is evanescent, and we can pick a maximum value for K_1 and K_2 such that exponential term is suitably small. In this work, the method defined in the appendix of Holland *et al.* (2012) was used to compute the upper limit to K_1 and K_2. If the seafloor contains layers with sound speed less than c_w, then the D_1 and D_2 terms can exhibit peaks when K_1 or K_2 is greater than k_w. Thus, we pick the greater of the limit based on the exponential decay, or $1.25 \times \omega/\min(\tilde{c}_p)$, where $\min(\tilde{c}_p)$ is the minimum phase speed of the sediment stack. This choice of upper limit was found to be sufficient for the scenarios examined in this work.

Once the upper limit of the horizontal wavenumbers has been chosen, the domain of support for the integral is meshed with triangles or squares. The integral can be computed for each mesh element, and then summed, as recommended by Iserles *et al.* (2006). The instantaneous frequency of the oscillations is proportional to the gradient of the phase function, η. For this problem, the gradient is small when K_1 and K_2 are close to zero and grows without bound as K_1 and K_2 approach k_w (for real values of k_w). This behavior can lead to errors and suboptimal speedup if a mesh with constant size was used for the entire domain.

To deal with the change in the phase gradient with wavenumber, the mesh size was refined as $\nabla\eta$ increased. This was implemented by first sampling the vertical wavenumber interval $[k_w, 0]$ with equally spaced points to create a vector in k_z space. These points were converted to points in the horizontal wavenumber space by using the formula, $K_1 = \sqrt{k_w^2 - k_z^2}$, which creates a vector of horizontal wavenumber points for the oscillatory part. The evanescent component was created by sampling the interval $k_z = i[0, k_w]$, and converting to the horizontal wavenumber using the same equation. An example of the sampled horizontal wavenumber is illustrated in Fig. 4. Note that the spacing between subsequent samples decreases as K_1 approaches k_w from both above and below and increases away from it.

Sampled wavenumber axes were created for both the K_1 and K_2 integration variables and were combined into a 2D grid by forming their tensor product. These points were then used to create a triangular mesh. Mesh elements that fell entirely outside the domain of support of the H_1 and H_2 functions were discarded. If an element intersected the

https://doi.org/10.1121/10.0000570

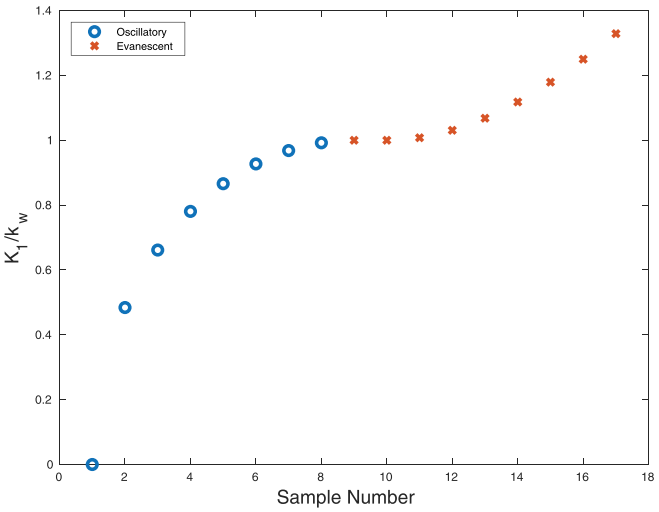

FIG. 4. (Color online) An illustration of the nonlinear sampling of the horizontal wavenumber axes. The vertical axis shows the sampled horizontal wavenumber normalized by the real part of the wavenumber in water, and the horizontal axis shows the sample number. Circles denote the oscillatory part, and crosses denote the evanescent part.

domain of support, the points outside the boundary were moved to the boundary. To handle the singularities in the H_1 and H_2 functions, a small portion near the edge of the boundaries is meshed with rectangular elements, also with a varying mesh size. An example mesh is shown in Fig. 5. Given this mesh, any numerical integration technique can be used for each element, either direct quadrature or the Levin technique.

Although no results using direct numerical integration are presented here, a technique to compute these is briefly described since the techniques to handle singularities are also used in the fast Levin technique. Each triangle in Fig. 5

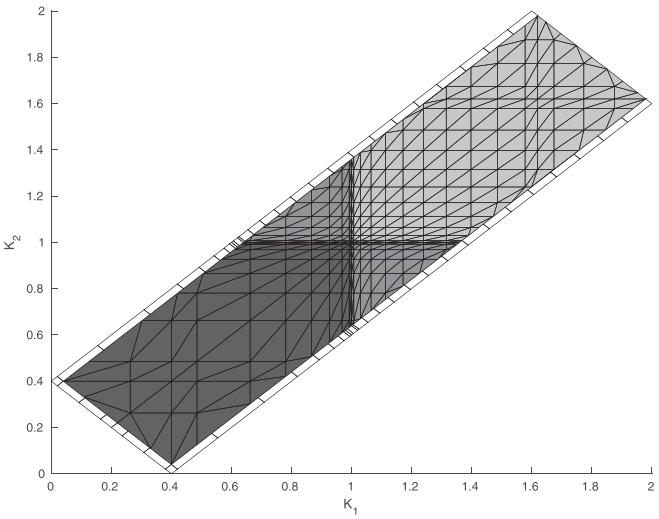

FIG. 5. An illustration of the mesh used to sample the wavenumber domain. The value of K is set to 0.4 rad/m as in Fig. 2. The elements shaded with the darkest gray color are completely oscillatory. Elements shaded with medium gray are oscillatory in one variable and evanescent in another. Elements shaded with the lightest gray are completely evanescent. The elements with no shading denote the singular boundary.

has a nonsingular (regular) integrand; therefore, it can be computed using standard 2D Gauss quadrature, wherein the integrand is sampled at various points within the triangle, multiplied by weights, and then summed. For such an implementation, the formulas tabulated by Cools and Rabinowitz (1993) could be used, for example.

For elements bordering the singular boundary, standard integration rules converge very slowly since the integrand is weakly singular with $O(x^{-1/2})$, where x is the distance from the boundary. To speed up convergence, the integral was transformed from (K_1,K_2) space into new coordinates, (u,v), where the Jacobian of the transformation regularizes the singularity. This process is performed by first transforming K_1 and K_2 to variables u', v' that are parallel and perpendicular to the singular boundary, respectively, with $v' = 0$ or $u' = 0$ being on the boundary (depending on the orientation). Then, the primed variables are transformed to u,v such that the coordinate normal to the singular boundary is mapped to the square root of itself. For most of the singular elements, only one edge is singular. Elements at the corners have two singular edges and both u' and v' are mapped to their square roots. These variable transformations allow the integral to be computed as

$$Q = \int\int \mathrm{d}u\mathrm{d}v\,[\phi(K_1(u,v),K_2(u,v))J]e^{iq\eta(K_1(u,v),K_2(u,v))}, \tag{21}$$

where J is the determinant of the Jacobian matrix, $\tilde{J}$, given by

$$\tilde{J} = \begin{bmatrix} \dfrac{\partial K_1}{\partial u} & \dfrac{\partial K_2}{\partial u} \\ \dfrac{\partial K_1}{\partial v} & \dfrac{\partial K_2}{\partial v} \end{bmatrix}. \tag{22}$$

The H_1 and H_2 functions have three singular boundaries, and a different transformation was used depending on which boundary the element was situated. This was implemented in our software by testing whether the vertices of each element intersected each boundary. Let boundary 1 be along the line $K_2 = K_1 - K$, boundary 2 be along the line $K_2 = K_1 + K$, and boundary 3 be along the line $K_2 = -K_1 + K$. We denote the different transformed variables as u_i,v_i for transformations for elements bordering a single boundary, i, with i ranging from 1 to 3. If the element borders on two boundaries, then the variables are denoted u_{ij},v_{ij} where i and j denote the boundaries. The meshing technique ensured that elements can only border on boundary 1 and 3, or 2 and 3. The variable transformations are

$$u_1 = \frac{1}{2}(K_1 + K_2), \tag{23}$$

$$v_1 = \sqrt{-K_1 + K_2 + K}, \tag{24}$$

$$u_2 = \frac{1}{2}(K_1 + K_2), \tag{25}$$

$$v_2 = \sqrt{K_1 - K_2 + K}, \tag{26}$$

$$u_3 = \sqrt{K_1 + K_2 - K}, \tag{27}$$

$$v_3 = K_1 - K_2, \tag{28}$$

$$u_{13} = \sqrt{(K_1 + K_2 - K)/2}, \tag{29}$$

$$v_{13} = \sqrt{-K_1 + K_2 + K}, \tag{30}$$

$$u_{23} = \sqrt{(K_1 + K_2 - K)/2}, \tag{31}$$

$$v_{23} = \sqrt{K_1 - K_2 + K}. \tag{32}$$

The Jacobian matrices corresponding to these transformations can be computed analytically.

If these variable transformations are applied to triangular elements, the element shape is distorted. On the other hand, rectangles with sides parallel and perpendicular to the singular boundary are mapped to rectangles in (u,v) space. This invariance is the reason for which rectangular elements are used for the weakly singular border. Standard 2D quadrature routines can then be applied to the integrand in (u,v) space.

V. FAST LEVIN INTEGRATION

When the oscillation parameter q becomes large, the direct integration techniques developed in Sec. IV require many integration points per element. Consequently, the computational cost becomes quite large. In this section, we use 2D Levin-type integration over each element to reduce the computational cost (Levin, 1982). An algorithm for computing the Levin method over general domains was developed by Olver (2006) and specialized here to triangles and rectangles. Although a 2D algorithm is given in Levin (1982), it is only valid for rectangular domains whose sides are parallel to the independent variable axes.

Levin's integration technique involves solving a non-oscillatory differential equation whose terms involve ϕ, q, and η. For 2D integrals, this technique is used to convert the 2D integral to a one-dimensional (1D) integral over the boundary via Stokes' theorem. Then, the 1D technique is used to convert the integral over each boundary segment to an evaluation at the endpoints via the fundamental theorem of calculus. Since 2D Levin integration requires application of the 1D version, the 1D version will be described first.

A. 1D Levin integration

The 1D Levin integration method computes integrals of the type (Levin, 1982)

$$Q_1 = \int_{y_l}^{y_u} \mathrm{d}y\, \phi(y) e^{iq\eta(y)}, \tag{33}$$

where y is a generic variable of integration. This technique relies on the basic idea that if a function $F(y)$ could be found that satisfies the equation

$$\phi(y) = \frac{\mathrm{d}F(y)}{\mathrm{d}y} + iq\frac{\mathrm{d}\eta(y)}{\mathrm{d}y}F(y), \tag{34}$$

then the integral in Eq. (33) can be computed by

$$Q_1 = F(y_u)e^{iq\eta(y_u)} - F(y_l)e^{iq\eta(y_l)}. \tag{35}$$

Since Eq. (34) has no complex exponentials, its oscillatory behavior has been significantly reduced.

Since a solution to this differential equation is rarely analytically available, it is solved numerically. We follow Levin (1982) and use the collocation method. Let y_p be a set of $p+1$ points in the interval $[y_l, y_u]$. Note that these points must include the endpoints in order to achieve the required asymptotic error, as noted by Levin (1982) referencing de Boor and Swartz (1973). Let v^p be a linear combination of p-order basis polynomials expressed as

$$v^p(y) = \sum_{j=0}^{p} d_j v_j^p(y), \tag{36}$$

where v_j^p is the jth-order basis function (with a maximum of p), and d_j are unknown coefficients.

If the basis functions are substituted in Eq. (34) and the collocation method is applied, then we obtain the linear algebra problem

$$Vd = \phi(y_m), \tag{37}$$

where d is a vector of unknown coefficients, d_j, V is a matrix with elements

$$V_{jm} = \frac{\mathrm{d}v_j^p(y)}{\mathrm{d}y}\bigg|_{y=y_m} + iq\left(v_j^p(y)\frac{\mathrm{d}\eta(y)}{\mathrm{d}y}\right)\bigg|_{y=y_m}, \tag{38}$$

where y_m is the mth collocation point of y_p, and v_j^p is the jth-order basis function. The linear system can be solved using standard techniques and the solution substituted into Eq. (35) by using v^p in place of F. This approximation is denoted by Q_{1p} for a pth-order polynomial approximation to the 1D integral in Eq. (33).

The approximate solution, Q_{1p} was shown by Olver (2006) to have an absolute error, $|Q_1 - Q_{1p}|$ of order $O(1/q)$ so long as the products $v_j^p\eta$ are linearly independent, and the points y_p include the endpoints of the interval. Since the magnitude of the integral $|Q_1|$ is asymptotically of order $O(1/q)$, the Levin method has constant relative error as a function of q with the constant depending on p. As the number of collocation points and the order of the polynomial function are increased, the accuracy for a given q increases. However, the matrix V can become poorly conditioned for very large numbers of basis functions or small values of q. In these cases, significant numerical errors arise if Gaussian elimination is used but can be mitigated by using a truncated singular value decomposition.

B. 2D Levin integration

The 2D Levin method exploits Stokes' theorem to convert the 2D integral over a domain into a set of 1D integrals

https://doi.org/10.1121/10.0000570

over its boundaries (Olver, 2006), which can then be solved using the 1D Levin method. To solve the 2D oscillatory integral in Eq. (18), we look for a vector function of two variables $\boldsymbol{F}(K_1,K_2) = (F_{K_1}(K_1,K_2), F_{K_2}(K_1,K_2))$ that satisfies the equation (omitting the function arguments for brevity)

$$\phi = \nabla \cdot \boldsymbol{F} + iq\nabla\eta \cdot \boldsymbol{F}, \tag{39}$$

where the divergence and gradient are in terms of K_1 and K_2.

Let y be the independent variable of the parametric curves $K_1(y), K_2(y)$ that describe the boundary, which in this case are piecewise-linear functions. Using Stokes' theorem, the 2D integral can be converted to the 1D integral

$$Q = \int \mathrm{d}y e^{iq\eta(K_1(y),K_2(y))}\left(F_{K_1}(K_1(y),K_2(y))\frac{\mathrm{d}K_2}{\mathrm{d}y} - F_{K_2}(K_1(y),K_2(y))\frac{\mathrm{d}K_1}{\mathrm{d}y}\right). \tag{40}$$

This is a 1D integral of the form Eq. (33) where the term in parentheses can be substituted for $\phi(y)$, and solved using the 1D Levin method. For the triangular and rectangular elements used in this work, this integral is computed for each straight line segment constituting the boundary and then summed to obtain the integral over the element.

To perform these steps numerically, the vector function $\boldsymbol{F}$ is approximated using the collocation method. This time, 2D vector polynomials are used to construct the basis functions. If independent polynomials are used to construct F_{K_1} and F_{K_2}, then the resulting linear system will be undetermined. In this work, a scalar polynomial as a function of two dimensions of order p was constructed, $v^p(K_1,K_2)$. It was converted into a vector by multiplying by the constant $\boldsymbol{\xi} = (\xi_1,\xi_2)$, where $|\boldsymbol{\xi}| = 1$. Orthogonal polynomials on the triangle were used as basis functions and computed using software accompanying Hesthaven and Warburton (2008).[1]

The 2D Levin method can suffer from numerical issues if the vector $\boldsymbol{\xi}$ is perpendicular to either $\nabla\eta$ or the element boundary as discussed in Olver (2006). Both of these cases can cause the columns of the matrix used in the linear system to be linearly dependent. This, in turn, causes the matrix to be poorly conditioned on the order of machine precision. To mitigate these effects, $\boldsymbol{\xi}$ was selected such that it was neither perpendicular to $\nabla\eta$ nor the boundary. Further discussion of these issues can be found in Olver (2006). For the singular elements, the Levin method must be modified to account for the weakly singular boundaries. The same variable transformation is used as for the direct quadrature technique. The Levin integration technique can be applied to the product (ϕJ) in (u,v) space.

In the direct integration method, 2D quadrature techniques can be selected such that all the evaluation points are in the interior of the element and not on the boundary. While the quadrature rule converges slowly, all function evaluations are finite. Levin's method, in contrast, requires evaluation at the endpoints to maximize the convergence rate (de Boor and Swartz, 1973; Levin, 1982). For singular elements, care must be taken to use the limit of ϕJ as points approach the boundary rather than evaluating ϕ and J and taking their product.

Since the Jacobian cancels out the singularity, the numerical approximation of this equation with orthogonal polynomials is appropriate. However, problems arise when computing the 1D boundary integrals that result from the application of Stokes' theorem. The transformation that cancels out the singularity warps the η functions such that its gradient is zero at endpoints that lie on the singular boundary. In this case, the columns of the matrix in the linear system are no longer linearly independent at the boundary point (Olver, 2007). To mitigate this problem, standard Gauss-Legendre quadrature is used for a small portion of the 1D integral near the stationary point (maximum of 10π of phase change in the exponential), and Levin integration is used for the rest of the integral.

VI. RESULTS AND DISCUSSION

In this section, the TDSS-L model output, $\langle|p(t)|^2\rangle$, computed using the technique described in Sec. V is presented for several environments: (1) a halfspace (either sand or mud), (2) a refracting mud layer over a sand halfspace, and (3) a turbidite sequence. In the first two scenarios, the TDSS-L model is compared with a sonar equation-type model. These model-model comparisons extend those performed by Tang and Jackson (2017) and provide additional evidence that the TDSS model is sound and the mathematics have been correctly implemented in the TDSS-L model, especially for the refracting mud layer case. The third scenario presents a considerably more complex sedimentary environment to demonstrate the TDSS model's ability to handle strongly layered seafloors. All of these scenarios use an altitude of $z_m = 4900$ m. The K_1,K_2 domain was meshed using 30 intervals between 0 and k_w, and 10th-order polynomials were used in the collocation method. Although results were not computed using quadrature, it is estimated that the cases at 200 Hz provide a speedup of 2 orders of magnitude, and at 4000 Hz, a speedup of 6 orders of magnitude compared to direct quadrature.

Simulations with a very large source/receiver altitude compared to the spatial resolution of the transmitted pulse will provide appropriate situations for comparison to the narrowband sonar equation. For the examples presented in Tang and Jackson (2017), small but noticeable differences were evident between the sonar equation models and the TDSS model (especially for the sand halfspace scenario) at an altitude of 200 m, center frequency of 200 Hz and temporal resolution (3 dB full width) of approximately 0.059 s. The temporal resolution of this pulse corresponds to an angular resolution on the seafloor of about 13° centered at 30° grazing angle. This large equivalent angular width of the transmitted pulse causes significant smoothing that can smear the critical angle peak. This same pulse has an angular

resolution of 0.5° at 30° grazing angle when a source/receiver altitude of 4.9 km is used. Therefore, deep water scenarios provide much less smoothing in angle for narrowband pulses. We focus here on narrowband pulses because broadband effects, such as the change in Bragg condition for each frequency, are included in the TDSS model but not in the narrowband sonar equation. Deep water environments and narrowband pulses provide cases in which the TDSS model should provide the same results as the narrowband sonar equation and, thus, constitute an appropriate test of the model physics in the TDSS model.

In the first two environments, comparisons are made to SCARAB, a sonar equation-based model that was developed to model the arrival structure and intensity of sub-bottom scattering (Holland and Neumann, 1998). It avoids the usual plane-wave approximation common to many sonar equation models by discretizing the sub-seabed into voxels and then summing in time the appropriately scaled and time-delayed scattered intensity from each voxel. It uses a ray approximation for the Green's function into and out of the sediment. It compares closely to a full-wave scattering model (LePage and Schmidt, 2003) where effects of caustics, multiple reflection from sub-bottom interfaces, and the evanescent field in the sediment are insignificant. The small-roughness perturbation approximation is used for the scattering cross section, and thus comparisons between the TDSS model and SCARAB cannot differentiate where the first-order perturbation term fails to sufficiently model the scattered field. These model-model comparisons, therefore, only test whether the TDSS model is modeling the correct propagation physics of a point source overlying a simple seafloor.

A. Scattering from a halfspace

A halfspace example using parameters appropriate for a sandy seafloor sound speed ratio $a_p = c_{p1}/c_w = 1.17/(1 + 0.0096i)$, and density ratio of $a_\rho = \rho_1/\rho_w = 2$ are shown in Fig. 6(a). Parameters are summarized in Table I. Attenuation in the seawater is not included in this or any of the following cases.

Comparisons to the sonar equation are made at three frequencies, 200 Hz, 1000 Hz, and 4000 Hz, to test whether the TDSS model gives the correct frequency dependence. Solid curves represent the TDSS-L model, and dotted-dashed black curves denote the narrowband sonar equation using perturbation theory. The model-model comparisons agree quite well, except for the onset of the pulse as it begins to interact with the bottom. Near the onset of the pulse, the two models agree for 200 Hz, but the sonar equation overpredicts this region as the frequency is increased to 1000 and 4000 Hz. If a smaller effective outer scale, L_{eff}, is used for the roughness spectrum, then a nearly perfect fit near pulse onset (specular direction) can be obtained with L_{eff} decreasing as the wavelength decreases. This effect is likely due to the Bragg condition being enforced exactly for all frequencies in the TDSS model, whereas it is only enforced in the scattering cross section at a single frequency for the sonar equation. Small oscillatory deviations in the TDSS model on the order of 0.1DB are present and can be decreased by refining the mesh used to integrate over the (K_1, K_2) domain. The peak at the critical angle at about 13 s is also well-modeled at all frequencies.

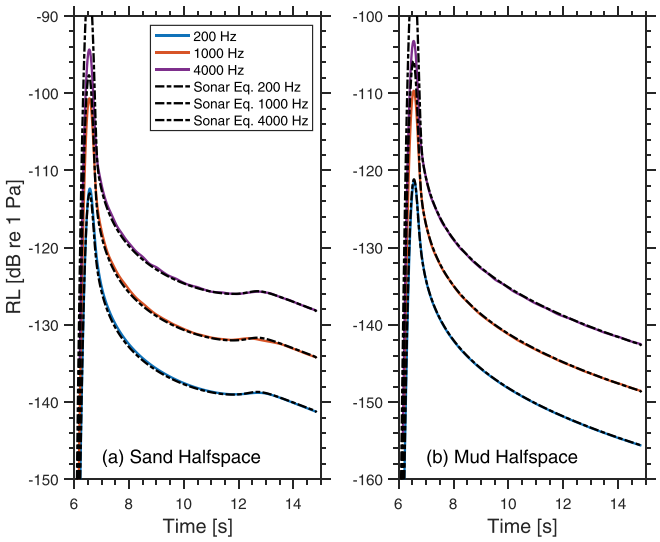

FIG. 6. (Color online) Model-model comparisons for the scattered mean square pressure from a sand (a) and mud (b) halfspace at 200 Hz, 1000 Hz, and 4000 Hz.

Comparisons for a halfspace using parameters appropriate for a muddy seafloor with $a_p = 0.98/(1 + 6841.7 \times 10^{-5} i)$ and $a_\rho = 1.4$ are presented in Fig. 6(b). Geoacoustic and roughness properties are summarized in Table I. The agreement between the two models is again excellent, except for the onset of the pulse, and correctly predicts the frequency dependence. Very slight oscillatory errors in the TDSS model are present, similar to the sand halfspace.

B. Scattering from a refracting layer

A more geologically realistic seafloor includes refraction in the sediment (due to increasing sound speed with depth), which is a good test of the physics in the TDSS model. The sound speed profile as a function of depth z (referenced to the water–sediment interface) is

$$\tilde{c}_p(z) = c_w \chi \left[(1+\beta)\sqrt{1 + \frac{2gz}{(\beta+1)\chi}} - \beta \right], \tag{41}$$

TABLE I. Geoacoustic and roughness parameters for the halfspace environment.

Parameter name	Units	Mud	Sand
Sound speed ratio	—	0.98	1.17
Density ratio	—	1.4	1.8
Attenuation	dB/m/kHz	10^{-3}	0.3
Spectral exponent	—	3	3
Spectral strength	$m^{4-\gamma_2}$	10^{-4}	10^{-4}
Outer scale	m	10	10

https://doi.org/10.1121/10.0000570

TABLE II. Geoacoustic and roughness parameters for the refracting layer environment.

Parameter name	Units	Mud	Sand
Sound speed ratio	—	0.98	1.13
Sound speed gradient	s^{-1}	1.3	—
Sound speed curvature	—	−0.5	—
Density ratio	—	1.4	2.0
Attenuation	dB/m/kHz	0.1	0.3
Spectral exponent	—	3	3
Spectral strength	$m^{4-\gamma_2}$	10^{-4}	1.2×10^{-3}
Outer scale	m	100	100

where $\chi = \tilde{c}_p(0)/c_w$ is the ratio between the sediment phase speed at the interface and the water sound speed, g is the sound speed gradient at the water–sediment interface in s^{-1}, and β is the curvature. This expression follows Hamilton's observation (Hamilton, 1980) that deep sea sediments exhibit a sound speed gradient of $O(10^0)s^{-1}$ at the water–sediment interface, which decreases with increasing depth in the sediment. For this test case, $\chi = 0.98$, $g = 1.3\ s^{-1}$, and $\beta = -0.5$. Geoacoustic and roughness properties for this environment are summarized in Table II. Only the water–sediment interface and mud–sand interface are rough.

The version of the TDSS model used in this work requires homogeneous layers, thus, here the profile is discretized into nine unevenly spaced layers, as seen in Fig. 7, to approximate a 100 m thick layer of mud overlying a sand halfspace. The narrowband sonar equation model, SCARAB, uses a ray approximation for the refracting sediment and finds eigenrays analytically for this sound speed profile (i.e., does not discretize the sound speed profile). Refraction in the mud changes the time-dependence of the mean square pressure scattered by the mud–sand interface by altering the local grazing angle of the field incident on that boundary, as well as increasing the ray path length through the mud.

The comparison between the TDSS-L model (a full-wave solution in a stratified medium) and SCARAB (ray approximation) for the refracting layer case is shown in Fig. 8. Figure 8(a) shows the contribution from the water–mud interface where excellent agreement is seen at 1000 and 4000 Hz, except for the onset of the pulse (as in the halfspace cases). At 200 Hz, oscillations are apparent in the TDSS-L model, but not in SCARAB. The TDSS model oscillations arise from fully coherent constructive and destructive interference between the water–sediment interface and sediment–basement interface reflections. The reflection coefficient [a crucial component of the scattered field manifest in the up- and down-going wave amplitudes, $A_n(K)$ and $B_n(K)$] is calculated with the assumption that each interface is flat (i.e., no roughness). Thus, the TDSS model overpredicts the effect of the oscillations (interference) since, in reality, the roughness would degrade/diminish the oscillation amplitude. SCARAB by contrast, assumes that scattering and reflection are both fully incoherent and thus underpredicts the effect of the oscillations (interference). In summary, neither model treats this problem exactly, but both can be considered as end members for the fully coherent/incoherent approximation to the scattered mean square pressures of a rough layer. Note that the oscillations are apparent in the TDSS model only at 200 Hz since the round trip attenuation through the mud layer is only 4 dB. At 1000 and 4000 Hz, the round trip attenuation is 20 and 80 dB, respectively, and thus does not lead to a detectable oscillation.

Figure 8(b) shows scattering from the mud-sand (basement) boundary. At 200 Hz, the TDSS model oscillations are much weaker than those from the water–mud interface but occur for the same reasons. The agreement between the two models at 1000 and 4000 Hz is very good. Finally, we

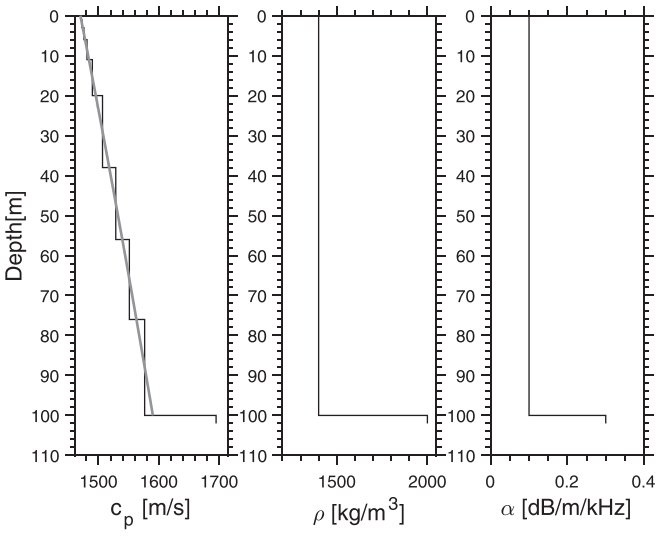

FIG. 7. Sediment geoacoustic profile for a refracting mud layer overlying a sand halfspace. In the plot for the sediment sound speed, c_p, the profile used for the TDSS model is shown as a black staircase, whereas the profile used for SCARAB is gray and continuously varying. Depth on the vertical axis is referenced to the water–sediment interface.

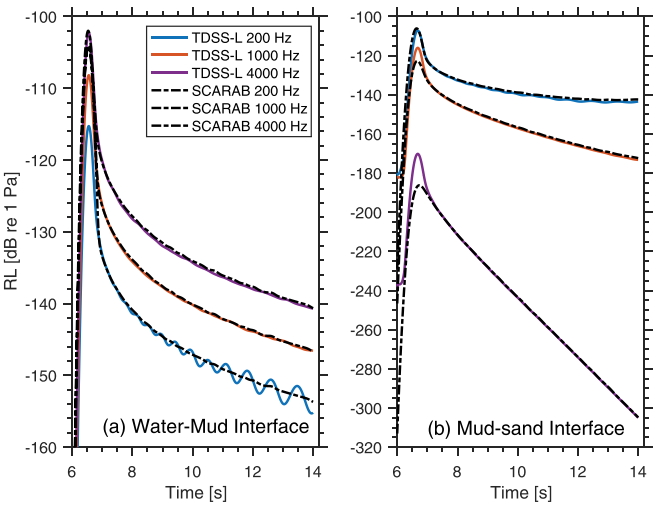

FIG. 8. (Color online) Comparison of the TDSS model with SCARAB for the refracting case (geoacoustic profile shown in Fig. 7) for (a) water–mud interface, and (b) mud–sand interface.

note that the slight fluctuations in SCARAB are discretization artifacts and can be reduced by finer sampling of the environment in range.

C. Scattering from a turbidite sequence

Abyssal plains cover a huge portion (more than 50%) of the Earth's surface. They are composed of alternating fine-grained and coarse-grained sediment layers, termed turbidite sequences (see, for example, Middleton, 1993). The fine-grained (muddy) layers come from the constant but slow deposition of pelagic particles. The coarse-grained silts and sands come from episodic seismically induced underwater avalanches of silt and sand from the continental shelf. Turbidite sequences occur in many different geologic settings, but here we consider a case from an abyssal plain where an individual pelagic or terrigenous layer is typically $O(10^{-1}$–$10^{0})$ m thick, and the total sediment thickness is typically $O(10^{3})$ m, although we only use a 100 m thick sediment here.

The effect of turbidites on acoustic reflection is profound and a strong function of frequency. At sufficiently low frequencies, the alternating pelagic/terrigenous sequence can be treated as an effective medium. At higher frequencies, the reflection coefficient increases dramatically, and the layering must be accounted for explicitly (Holland and Muncill, 1993). In Holland and Muncill (1993), a simplified stochastic model of a turbidite sequence successfully explained the measurements in which the pelagic layer thickness followed a gamma function distribution, but the terrigenous layer thickness was fixed. Here, the probability density function V for the pelagic (mud) layer thickness, ℓ is $V(\ell) = \ell \exp(-2\ell/\mu)/(\mu/2)^2$, where μ is the mean of the distribution and the standard deviation is $\mu/\sqrt{2}$. It was also found in Holland and Muncill (1993) that including the sound speed depth dependence was important for both layers. Here, the sound speed profile follows Eq. (41) with the same parameters as in the refracting case. This is the geoacoustic model used to generate Fig. 9 with parameters given in Table III. Roughness parameters are also given in Table III. For all interfaces within the sediment sequence, including the basement, the sand roughness parameters are used. At the water–mud interface, the mud parameters are used.

TABLE III. Geoacoustic and roughness parameters for the turbidite environment.

Parameter name	Units	Mud	Silt
Mean layer thickness	m	1	0.25
Interface sound speed ratio	—	0.98	1.053
Density	kg/m^3	1400	1800
Attenuation	dB/m/kHz	0.01	0.1
Sound speed gradient	s^{-1}	1.3	1.3
Spectral strength	m$^{4-\gamma_2}$	1×10^{-4}	1.2×10^{-3}
Spectral exponent	—	3.0	3.0
Outer scale	m	10	10

Results from the TDSS-L model are shown for this environment, but not for SCARAB since the ray approximation therein will fail for layer thicknesses smaller than a wavelength. These results model multiple reflections due to the background layering exactly, but assume there is no effect on the coherent field due to the roughness. Multiple scattering between different rough interfaces is ignored, which may be an important factor in scattering from these environments. The total mean square pressure due to all (summed) rough layers is shown in Fig. 10. Note that the mean square pressure versus time is relatively smooth at 200 Hz, while at 1000 and 4000 Hz, significant oscillations are evident despite the TDSS model yielding a formal average over roughness. For wavelengths much greater than the mean layer thickness, i.e., at 200 Hz, the layered medium behaves as an effective medium, similar to that for the reflection coefficient (Holland and Muncill, 1993).

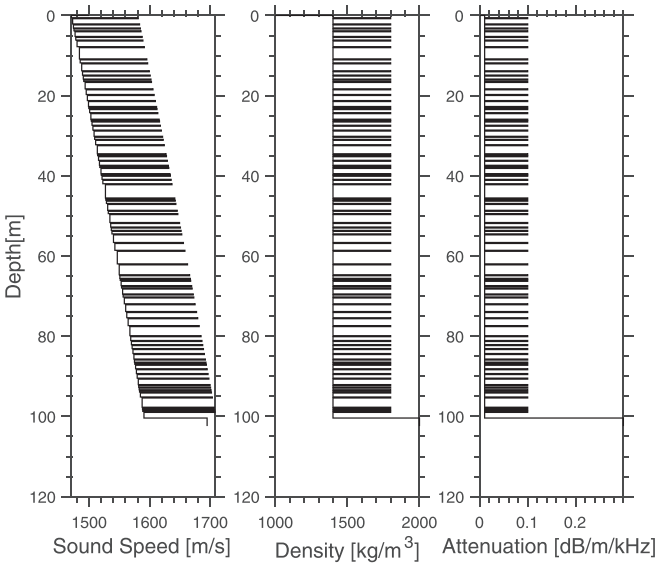

FIG. 9. Sediment geoacoustic profile for a turbidite environment. The depth on the vertical axis is referenced to the water–sediment interface.

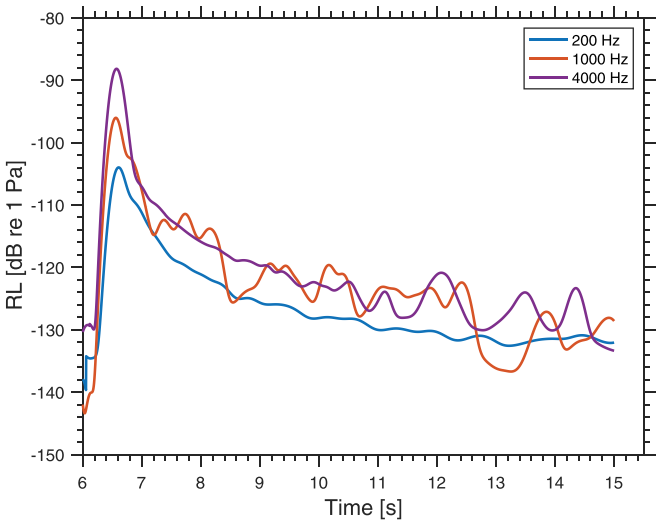

FIG. 10. (Color online) Scattered mean square pressure from a deep water turbidite sequence.

https://doi.org/10.1121/10.0000570

However, as frequency increases, stop- and passbands emerge as a result of the quasi-periodic sequence. In contrast to the other test cases (Figs. 6 and 8), where for times beyond the normal incidence (6.5 s) the received level increases monotonically at 3 dB/per octave, here, it is roughly the same at 1000 and 4000 Hz.

Although other aspects of the TDSS-L model predictions could be explored, the main purpose of exercising the TDSS-L model in this environment was to demonstrate its ability to treat challenging sedimentary environments, here, a finely layered random medium. In addition, this environment was computationally challenging for two reasons: the source/receiver height was large, $z_m = 4900$ m, and the number of layers, $N = 157$, was also large.

VII. CONCLUSION

Sediment interface roughness and volume heterogeneities exist across a broad range of scales, which leads to scattering of acoustic waves across a broad frequency range. Although sediment scattering models based on a plane-wave incident field have a relatively low computational cost, full-wave models needed to interpret measurements, i.e., treat a point source, have a very high computational cost. The computational cost is so high that they have been impractical for interpreting measurements in deep ocean environments. We show a method for substantively reducing the computational cost of the wavenumber integration-based TDSS model (Tang and Jackson, 2017), using methods developed by Levin (1982) and Olver (2006). There are hurdles to applying the Levin method to the TDSS model, for example, the presence of singularities and nonlinear phase terms in the integrand. Detailed solutions to these hurdles are provided.

Several deep water test cases were used to validate the computationally efficient model, TDSS-L. Comparisons indicated that the underlying theory for the TDSS model and its numerically efficient implementation here are correct, especially for the nontrivial case of a refracting mud sediment layer. These cases extend those presented in Tang and Jackson (2017), and demonstrate better agreement between the TDSS model and the sonar equation. A case was also presented with a complex random turbidite sequence, which demonstrates some of the potential of the TDSS model, since it is an environment that the narrowband sonar equation is not expected to model exactly. For these problems, the computational cost was reduced by between 2 and 5 orders of magnitude over standard quadrature methods, depending on the frequency.

Up to now, standard deep water scattering measurements (with source and receiver depths small with respect to water depth) could generally only be analyzed with ray-based models. While ray-based models are reasonably accurate in simple environments, they cannot treat the more complex seabed structure. The reduction in computational cost for this full-wave scattering model opens the door to a more complete understanding of deep ocean sediment heterogeneities that lead to scattering.

The computational approach detailed here renders deep ocean calculations practical up to frequencies in the thousands of hertz. The approach was demonstrated for rough surfaces but can be directly applied to volume heterogeneities. The approach can also be applied to other scattering models based on wavenumber integration.

ACKNOWLEDGMENTS

We thank the Office of Naval Research for financial support of this work. We also thank D. J. Tang and Darrell Jackson for helpful discussions.

[1]Available at https://github.com/tcew/nodal-dg under the MIT license (Last viewed 14 January 2019).

Cools, R., and Rabinowitz, P. (**1993**). "Monomial cubature rules since "troud": A compilation," J. Comp. Appl. Math. **48**(3), 309–326.
de Boor, C., and Swartz, B. (**1973**). "Collocation at Gaussian points," SIAM J. Numer. Anal. **10**, 582–606.
Hamilton, E. L. (**1980**). "Geoacoustic modeling of the sea floor," J. Acoust. Soc. Am. **68**(5), 1313–1340.
Hellequin, L., Boucher, J. M., and Lurton, X. (**2003**). "Processing of high-frequency multibeam echo sounder data for seafloor characterization," IEEE J. Ocean Eng. **28**(1), 78–89.
Hesthaven, J. S., and Warburton, T. (**2008**). *Nodal Discontinuous Galerkin Methods: Algorithms, Analysis, and Applications* (Springer, New York).
Holland, C. W., and Muncill, G. (**1993**). "Acoustic reflection from quasiperiodic sedimentary sequences," J. Acoust. Soc. Am. **94**(3), 1609–1620.
Holland, C. W., and Neumann, P. (**1998**). "Sub-bottom scattering: A modeling approach," J. Acoust. Soc. Am. **104**(3), 1363–1373.
Holland, C. W., Nielsen, P. L., Dettmer, J., and Dosso, S. (**2012**). "Resolving meso-scale seabed variability using reflection measurements from an autonomous underwater vehicle," J. Acoust. Soc. Am. **131**(2), 1066–1078.
Iserles, A., Nørsett, S., and Olver, S. (**2006**). "Highly oscillatory quadrature: The story so far," in *Numerical Mathematics and Advanced Application*, edited by D. de Gómez, P. Quintela, and P. Salgado (Springer, Berlin).
Ivakin, A. N. (**1998**). "A unified approach to volume and roughness scattering," J. Acoust. Soc. Am. **103**(2), 827–837.
Jackson, D. R., and Richardson, M. D. (**2007**). *High-Frequency Seafloor Acoustics*, 1st ed. (Springer, New York).
Jensen, F. B., Kuperman, W. A., Porter, M. B., and Schmidt, H. (**2011**). *Computational Ocean Acoustic* (Springer, New York).
Kuo, E. Y. T. (**1964**). "Wave scattering and transmission at irregular surfaces," J. Acoust. Soc. Am. **36**(11), 2135–2142.
LePage, K. D., and Schmidt, H. (**2000**). "Spectral integral representations of volume scattering in sediments in layered waveguides," J. Acoust. Soc. Am. **108**(4), 1557–1567.
LePage, K. D., and Schmidt, H. (**2003**). "Spectral integral representations of monostatic backscattering from three-dimensional distributions of sediment volume inhomogeneities," J. Acoust. Soc. Am. **113**(2), 789–799.
Levin, D. (**1982**). "Procedures for computing one- and two-dimensional integrals of functions with rapid irregular oscillations," Math. Comp. **38**(158), 531–538.
Levin, D. (**1996**). "Fast integration of rapidly oscillatory functions," J. Comput. Appl. Math. **67**(1), 95–101.
Middleton, G. V. (**1993**). "Sediment deposition from turbidity currents," Annu. Rev. Earth Planet. Sci. **21**(1), 89–114.
Morse, P. M., and Ingard, K. U. (**1968**). *Theoretical Acoustics* (Princeton University Press, Princeton, NJ).
Ogilvy, J. A. (**1991**). *Theory of Wave Scattering from Rough Surfaces* (Hilger, Bristol, UK).

Olver, S. (**2006**). "On the quadrature of multivariate highly oscillatory integrals over non-polytope domains," Numer. Math. **103**(3), 643–665.
Olver, S. (**2007**). "Moment-free numerical approximation of highly oscillatory integrals with stationary points," Eur. J. Appl. Math. **18**(4), 435–447.
Oppenheim, A. V., Schafer, R. W., and Buck, J. R. (**1999**). *Discrete-Time Signal Processing*, 2nd ed. (Prentice-Hall, Upper Saddle River, NJ).
Quijano, J. E., Dosso, S. E., Dettmer, J., and Holland, C. W. (**2015**). "Fast computation of seabed spherical-wave reflection coefficients in geoacoustic inversion," J. Acoust. Soc. Am. **138**(4), 2106–2117.
Schmidt, H., and Kuperman, W. A. (**1995**). "Spectral representations of rough interface reverberation in stratified ocean waveguides," J. Acoust. Soc. Am. **97**(4), 2199–2209.
Tang, D., and Frisk, G. V. (**1992**). "Spectral parametrization of scattering from a random ocean bottom," J. Acoust. Soc. Am. **92**(5), 2792–2799.
Tang, D., and Jackson, D. (**2017**). "A time-domain model for seafloor scattering," J. Acoust. Soc. Am. **142**(5), 2968–2978.
Tatarski, V. I. (**1961**). *Wave Propagation in a Turbulent Medium* (Dover, New York).
Watson, G. N. (**1944**). *A Treatise on the Theory of Bessel Functions*, 2nd ed. (Cambridge University Press, New York).